

# Subwavelength precision optical guiding for trapped atoms coupled to a nanophotonic resonator

Xinchao Zhou,<sup>1,\*</sup> Hikaru Tamura,<sup>1,\*</sup> Tzu-Han Chang,<sup>1</sup> and Chen-Lung Hung<sup>1,2,†</sup>

<sup>1</sup>*Department of Physics and Astronomy, Purdue University, West Lafayette, IN 47907, USA*

<sup>2</sup>*Purdue Quantum Science and Engineering Institute,  
Purdue University, West Lafayette, IN 47907, USA*

(Dated: November 2, 2021)

We demonstrate an efficient optical guiding technique for trapping cold atoms in the near field of a planar nanophotonic circuit, and realize atom-photon coupling to a whispering-gallery mode in a microring resonator. The guiding potential is created by diffracted light on a nanophotonic waveguide that smoothly connects to a dipole trap in the far field for atom guiding with subwavelength precision. We show that the guided atoms can be localized in a tight optical trap in the near field without further cooling. We observe atom-induced transparency for light coupled to a microring, characterize the atom-photon coupling rate, and extract guided atom flux as well as trap loading probability. Our demonstration promises new applications with trapped atoms on a nanophotonic circuit for quantum optics and quantum technologies.

Localized atoms strongly coupled to photonic fields are model systems for realizing quantum nonlinear optics [1], quantum networks [2, 3], and quantum simulations of many-body physics [4–6]. Interfacing trapped atoms with nanoscale photonic waveguides [7–14] and resonators [15–26] in quasi-linear (1D) and planar (2D) geometries further promises stronger atom-light interactions and novel quantum functionalities via dispersion engineering, controlled photon propagation, topology, and chiral quantum transport, thus leading to new paradigms for quantum optics beyond conventional settings in cavity and waveguide quantum electrodynamics (QED) [27, 28].

To date, the key challenge for atom-nanophotonic integration remains to be efficient trapping of cold atoms on nanoscale dielectrics. Success so far has been limited to suspended 1D structures, which are surrounded by vacuum and allow for laser-cooled atoms to be loaded directly into optical traps in the near field (distance  $z \lesssim$  optical wavelength above surface). Examples include optical nanofibers [7, 8], where an array of atoms can be localized in a lattice of two-color evanescent field traps formed by guided light. Through external illumination, a tight optical trap can also form on top of a suspended waveguide [14, 15, 22]. For deterministic atom trapping, optical tweezers or an optical conveyor belt have been utilized to initiate atom loading in freespace, followed by transport to a proximal photonic crystal [15, 29]. These trapping techniques enable demonstrations of cooperative atom-photon coupling [9–11, 14], and collective Lamb shifts with trapped atoms [30]. Waveguide-interfaced atomic quantum memories [12], photonic phase gate [17], and atom-photon/atom-atom entanglement [26] have also been realized.

Extending optical trapping to 2D photonic structures, however, faces immediate challenges. Due to restricted

trap opening to freespace and reduced laser cooling efficiency above a dielectric plane, unobstructed atom loading into a near field trap has shown limited success probability [31, 32]. This has prevented further explorations of atom-light coupling on more complex and interesting planar structures such as 2D photonic crystals [33].

In this letter, we overcome such restrictions using a simple trapping technique for precision guiding of cold atoms from far field ( $z \gtrsim 250 \mu\text{m}$ ) to a nanoscale optical trap in the near field with subwavelength precision. This scheme is projected to work with generic dielectric nanostructures – a far-off resonant optical beam forms a tapered guiding potential towards a bottom-illuminated structure (Fig. 1), where diffracted light in the near field can precisely direct trapped atoms towards the surface like a geometrically defined ‘optical funnel’. We show that the end of an optical funnel ( $z \lesssim 100 \text{ nm}$ ) can be plugged using a repulsive evanescent field potential that could also counteract atom-surface Casimir-Polder attraction to form a stable trap [Fig. 1(d)].

We implement an optical funnel for guiding and trapping cold atoms, for the first time, on a nanophotonic microring resonator in a fiber-integrated circuit [34, 35]. We achieve synchronous atom guiding towards a designated spot on a microring, and report observation of atom-photon coupling in a whispering-gallery mode (WGM) of the microring resonator. We extract a peak atom flux  $\approx 161 \text{ ms}^{-1}$ , under an averaged peak atom-photon coupling rate  $\bar{g}_{\text{max}}/(2\pi) \approx 90 \text{ MHz}$  for an unpolarized atom. To further trap a guided atom, we ramp on a top-illuminating beam to form a deep surface trap and capture single atoms with  $\approx 10\%$  probability at  $z \approx 220 \text{ nm}$  without further cooling. Our scheme is simpler than an optical conveyor belt [29, 31], and can be extended to trapping atom arrays in generic planar nanostructures.

We begin the experiment by collecting  $\sim 10^5$  polarization gradient-cooled (PGC) cesium atoms (temperature  $\sim 20 \mu\text{K}$ ) at  $z \approx 250 \mu\text{m}$  above a transparent silica membrane that hosts a racetrack-shaped  $\text{Si}_3\text{N}_4$  micror-

\* These authors contributed equally to this research.

† [chlung@purdue.edu](mailto:chlung@purdue.edu)

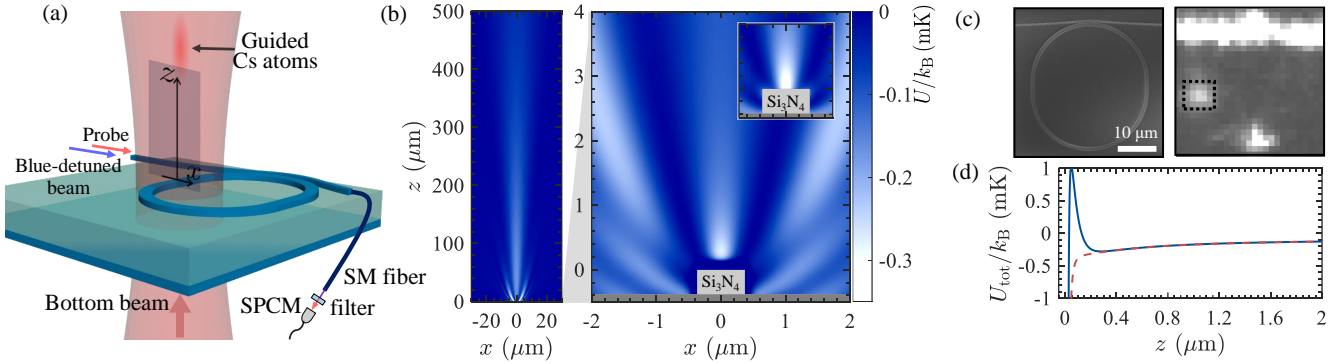


FIG. 1. Optical funnel on a nanophotonic microring circuit. (a) Schematic of the setup. An optical funnel is formed by a red-detuned, bottom-illuminating beam. WGMs in the microring are excited by a probe field co-propagating with a blue-detuned beam. The latter forms a repulsive potential barrier to plug the optical funnel. Transmitted light is directed to a single photon counting module (SPCM) after wavelength filtering. (b) Cross section of the funnel potential  $U(x, z)$  (left) and a zoom in view near the  $\text{Si}_3\text{N}_4$  waveguide (right). Inset shows the potential without a barrier (unplugged funnel). (c) Scanning electron micrograph of a microring (left), and an optical micrograph (right, same field of view) showing fluorescence from guided atoms (bounded by dashed box). (d) Potential line cuts  $U_{\text{tot}}(0, z)$  with (solid curve) and without (dashed curve) the repulsive barrier.  $U_{\text{tot}} = U + U_{\text{cp}}$  includes the atom-surface Casimir-Polder potential  $U_{\text{cp}}$  [35].

ing resonator [35, 36]. The atoms are loaded into an optical funnel that points towards the microring waveguide of width  $\approx 750$  nm and height  $\approx 380$  nm, respectively. The funnel potential is formed in a red-detuned, bottom-illuminating beam (wavelength  $\lambda_r \approx 935.3$  nm), with a beam waist of  $7 \mu\text{m}$  and a polarization locally parallel to the waveguide. Over the top, the zeroth-order diffraction exhibits strong intensity gradient, diffracting from a  $200$  nm  $1/e^2$ -transverse width into a circular far-field dipole beam profile; see Fig. 1(b) and [35]. Higher order diffractions do not form funnels because they display intensity maxima that are several micrometers away from the waveguide. Localized atoms in the optical funnel can be fluorescence imaged at distances  $z \lesssim 10 \mu\text{m}$  [31, 32], as shown in Fig. 1(c).

We plug the optical funnel using a repulsive evanescent field formed by a ‘blue’ WGM (wavelength  $\lambda_b \approx 849.1$  nm). A plugged funnel potential exhibits a stable trap minimum in the near field. We adjust the power of the bottom beam,  $P_r \approx 15 \text{ mW}$ , and that of the blue-detuned beam,  $P_b \approx 40 \mu\text{W}$ , to form a closed trap with trap minimum at  $z \approx 280$  nm and a trap depth of  $k_B \times 250 \mu\text{K}$ , where  $k_B$  is the Boltzmann constant; see Fig. 1(d).

We detect guided atoms in the near field by probing atom-WGM photon interactions. The ‘probe’ WGM resonance is thermally stabilized to the  $F = 4 \leftrightarrow F' = 5$  transition in D2 line. Probe photons are sent through one end of a bus waveguide to couple to the clockwise circulating (CW) WGM (coupling rate  $\kappa_e \approx 2\pi \times 2.3 \text{ GHz}$ ). The intrinsic photon loss rate is  $\kappa_i \approx 2\pi \times 4.8 \text{ GHz}$ , and the total photon loss rate is  $\kappa = \kappa_e + \kappa_i \approx 2\pi \times 7.1 \text{ GHz}$  [35]. Resonant probe photons are drawn into the microring and dissipate, reducing the bus waveguide transmission to  $T_0 = |(\kappa_e - \kappa_i)/\kappa|^2 \approx 0.1$ . Interaction with an atom will lead to an increased transparency  $T > T_0$

[35, 37]. We note that a WGM photon is nearly circularly polarized in the near field. Interaction with the probe WGM (in CW circulation) can thus drive  $\sigma^+$  transitions with spin axis defined transversely to the waveguide; the counter-clockwise circulating (CCW) WGM, on the other hand, drives  $\sigma^-$  transitions [35]. In our microring, CW and CCW WGM resonances are degenerate.

Our probe sequence is illustrated in Fig. 2(a) inset. We prepare atoms in the  $F = 4$  ground state and then shut off the PGC light, allowing them to be guided towards the microring surface. After a wait time  $\Delta t$ , two weak probe pulses are sent through the bus waveguide, each with a duration of 1 ms, to measure the transmission  $T$  ( $T_0$ ) in the presence (absence) of atoms; the bottom beam is switched off for 3 ms between the two pulses to release guided atoms. Each experiment is repeated for 100 times for averaging.

In Fig. 2(a), we observe increased transmission and a clear maximum at  $\Delta t \approx 3.5$  ms, indicating a peak atom flux arriving at the near field. Interestingly, transmission resurges at  $10 \text{ ms} \lesssim \Delta t \lesssim 16 \text{ ms}$ . Similar oscillatory behavior can also be found in atomic fluorescence [35] with a period of  $\sim 9$  ms, roughly matching half of the longitudinal trap period of the bottom beam potential. This suggests guided atoms are reflected longitudinally and are drawn back towards the surface for recoupling. For atom guiding without the repulsive barrier, observed transmission increase is less pronounced. However, oscillations in atomic fluorescence remain visible [35].

We find that atoms reflect longitudinally in the funnel for two main reasons. One is apparently due to the repulsive barrier in the plugged funnel. The other one arises from rapid tapering of the guiding potential within  $z \lesssim 20 \mu\text{m}$  [35]. When a guided atom experiences strong transverse compression, it would quickly gain transverse kinetic energy while reducing the longitudinal kinetic en-

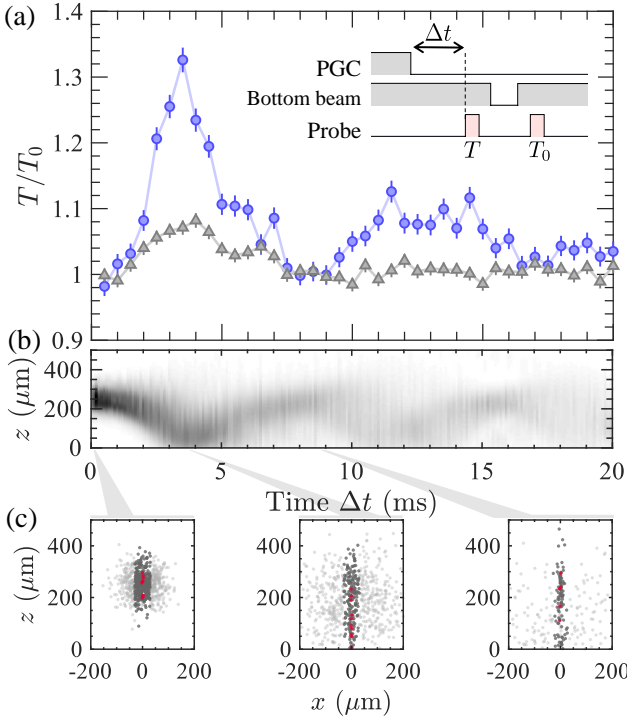


FIG. 2. Atom guiding in the optical funnel. (a) Resonant transmission  $T/T_0$  versus guiding time  $\Delta t$  in a plugged (circles) and unplugged (triangles) funnel, respectively. Experimental sequence is illustrated in the inset. (b) Normalized atomic distribution along the  $z$  axis, evaluated by Monte Carlo trajectory calculations using the experimental initial conditions. (c) Sample trajectory distributions at the indicated timing. Dark gray (light gray) circles mark those initially loaded (not loaded) in the funnel potential, while red circles label those entering the near field.

ergy according to the classical adiabatic theorem [38, 39]. This results in longitudinal deceleration that can even reflect an atom before it approaches the near field.

Our atomic trajectory simulations [40] confirm the observed guiding effect. In Fig. 2(b), simulated density near the waveguide surface ( $z \approx 0$ ) shows quasi-periodic oscillations that align well to the observed oscillatory peaks in Fig. 2(a). Within those guided trajectories,  $\sim 6\%$  near the center ( $x \approx 0$ ) and with a small initial transverse velocity can be directed to the near field [Fig. 2(c)]. Compared with free-falling cases, the number of atoms arriving on the waveguide is estimated to increase by 40 times with optical guiding.

The repulsive barrier can further increase the atom-WGM photon interaction time. Figure 3(a) overlays sample trajectories and position-dependent atom-CW WGM photon coupling strength  $\bar{g}$ , calculated using the mode field distribution [41] and averaged over  $g$  of all magnetic sub-levels [35]. Note that  $\bar{g}$  is constant along the waveguide ( $y$ -axis). Most trajectories exhibit a longitudinal classical turning point in the near field  $z = 110 \pm 20$  nm and within  $|x| \lesssim 0.3 \mu\text{m}$ . Corresponding time-dependent coupling strengths  $\bar{g}(t)$  are plotted in

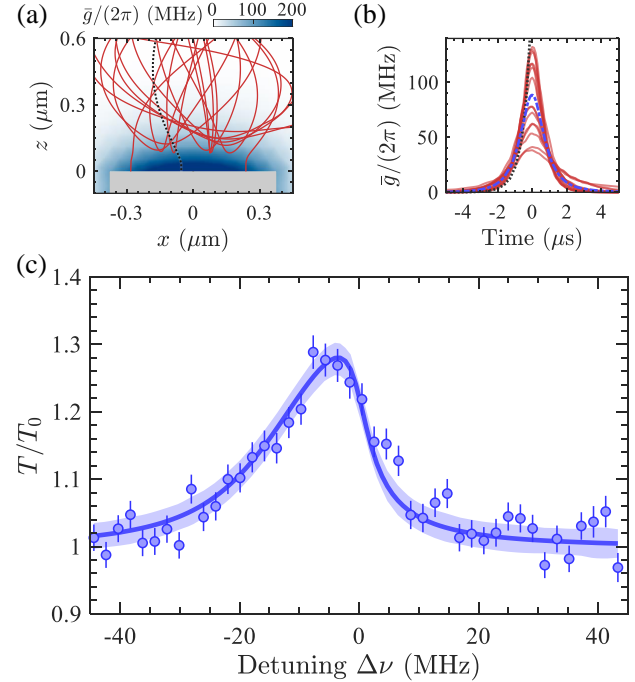


FIG. 3. Atom-WGM photon interaction. (a) Sample trajectories (solid curves) in the near field. False color map shows unpolarized atom-photon coupling strength  $\bar{g}$ . (b)  $\bar{g}$  versus time for sample trajectories; blue dash-dotted curve is the mean. Black dotted curves in (a-b) show a typical case without the repulsive barrier. (c) Measured transmission  $T/T_0$  versus laser detuning  $\Delta\nu$ . Solid curve is a single parameter fit using Eq. (1) and input from trajectory calculations as in (a-b). Shaded band shows 95% pointwise confidence level.

Fig. 3(b). Averaging over all trajectories, we find peak  $\bar{g}_{\max} \approx 2\pi \times 90$  MHz, corresponding to a peak cooperativity  $\bar{C} = 4\bar{g}_{\max}^2/\kappa/\gamma \approx 0.9$ . Here  $\gamma = 2\pi \times 5.2$  MHz is the atomic decay rate in freespace. The averaged interaction time (for the duration of  $\bar{g}(t)/\bar{g}_{\max} > 0.1$ ) would approach  $t_i \approx 3.5 \mu\text{s}$ , more than tripled from  $\sim 1 \mu\text{s}$  for typical trajectories without a repulsive barrier.

To experimentally characterize guided atoms in the near field, we vary the probe detuning  $\Delta\nu$  and measure the transmission spectrum at  $\Delta t = 3.5$  ms (Fig. 3). We notice that the measured peak transmission  $T/T_0 \approx 1.3$  is much smaller than the estimated steady-state transmission  $\approx |1 - 2\kappa_e(1 + \bar{C}^-)/[\kappa(1 + \bar{C}^+ + \bar{C}^-)]|^2/T_0 \approx 2.9$ , which assumes the averaged single-atom cooperativity is  $\bar{C}^+ = 0.9$  (and  $\bar{C}^- \approx 0.5\bar{C}^+$ ) for atom-CW (CCW) WGM coupling [35]. The reduced transparency is likely due to a finite atom flux  $\mathcal{N}$  and short interaction time  $t_i$  per atom transit, giving an effective atom number  $\mathcal{N}t_i < 1$ . Moreover, the apparent linewidth ( $\approx 20$  MHz) is slightly larger than the expected Purcell broadening  $\approx (1 + \bar{C}^+ + \bar{C}^-)\gamma/(2\pi) \approx 12$  MHz, and the spectrum is red-shifted by  $\approx 5$  MHz from freespace resonance ( $\Delta\nu = 0$ ).

The red shift and excess broadening can be explained by a state- and position-dependent light shift, which is

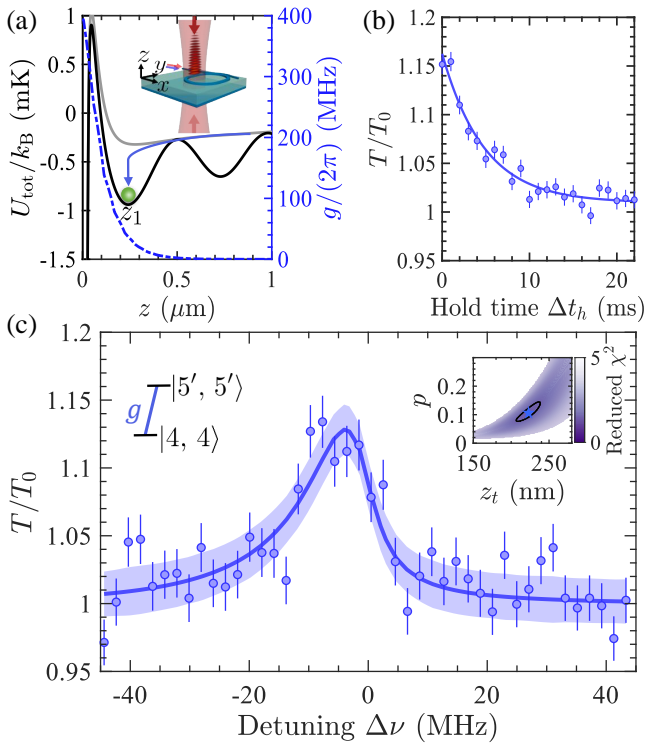


FIG. 4. Trapped atoms in a top-illuminating beam. (a) Potential linecuts  $U_{\text{tot}}(0, z)$  with (black) and without (grey) the top beam. Green circle indicates a trapped atom at the closest site ( $z_1$ ) near the surface. Dashed-dotted line shows the position-dependent coupling rate  $g$ . Inset illustrates the lattice potential created by the top beam. (b) Resonant transmission  $T/T_0$  and an exponential fit. (c) Transmission spectrum with trapped atoms. Solid line is a minimum  $\chi^2$  fit (see text), determining trap probability  $p$  and position  $z_t$  as shown in the inset; black ellipse marks 95% confidence region. Shaded band shows 95% pointwise confidence level.

primarily induced by the blue WGM that creates the repulsive barrier [35]. Whereas, there is negligible contribution from the attractive beam, because  $\lambda_r$  is near the magic wavelength for D2 transition [8]. Using trajectory calculations as shown in Fig. 3(a-b), we take into account time- and state-dependent coupling  $g(t)$  and light shift, respectively, and calculate a time-averaged transmission signal

$$\frac{T}{T_0} = 1 + \mathcal{N} \left[ \frac{\langle \int \mathcal{T}(\Delta\nu, g(t)) dt \rangle}{\int \mathcal{T}(\Delta\nu, 0) dt} - 1 \right], \quad (1)$$

where  $\mathcal{T}(\Delta\nu, g)$  is the steady-state transmission contributed from unpolarized magnetic sub-levels [35] and  $\langle \dots \rangle$  denotes averaging over trajectories. This model fits very well to the measured line shape, using the flux  $\mathcal{N}$  as the only adjustable parameter. We find  $\mathcal{N} = 161(4) \text{ ms}^{-1}$ , giving  $\mathcal{N}t_i \approx 0.56$ , that is, one coupled atom in half of the time during the probe window.

We further localize atoms in the optical funnel by synchronously ramping on a tight potential above the mi-

croing waveguide. As illustrated in Fig. 4(a), we illuminate the waveguide with a red-detuned beam from the top, with a matching waist as the bottom beam and a wavelength near  $\lambda_r$ . An optical lattice would form, due to interference between the top beam and its own reflection from the waveguide surface. Prior to trapping, we also polarize the atoms in the  $|F = 4, m_F = 4\rangle$  ground state. An atom, if present in the trap, can be interrogated by CW WGM photons with the  $|F = 4, m_F = 4\rangle \leftrightarrow |F' = 5, m_{F'} = 5\rangle$  cycling transition. The closest site to the waveguide is expected at  $z_1 \approx 243 \text{ nm}$  [Fig. 4(a)]. We expect large trap frequencies  $(\omega_x, \omega_y, \omega_z) \approx 2\pi \times (199, 19, 310) \text{ kHz}$  and an atom-CW WGM photon coupling rate  $g_1 \approx 2\pi \times 37 \text{ MHz}$ . Coupling rate in other trap sites is negligibly small ( $\lesssim 2\pi \times 0.2 \text{ MHz}$ ) and can be neglected.

We monitor the time-dependent transmission signal for hold time  $\Delta t_h$  following ramping on the top trap, in  $20 \mu\text{s}$ , at  $\Delta t = 3.5 \text{ ms}$ . Measured transmission signal now decays exponentially [Fig. 4(b)], indicating a trap lifetime of  $\tau = 4.0(6) \text{ ms}$  without further cooling.

Figure 4(c) shows the transmission spectrum with trapped atoms (at  $\Delta t_h = 0$ ). Peak  $T/T_0$  decreases from  $\approx 1.35$  (Fig. 3) to  $\approx 1.15$  due to a reduced probability  $p$  for trapping atoms in the near field and a reduced atom-photon coupling rate expected at  $z \approx z_1$ . The transmission spectrum can be similarly fitted by a model assuming a trapped atom at  $(x, z) = (0, z_t)$  with position variations  $\sigma_i = \sqrt{k_B T_t / (m\omega_i^2)}$  (for  $i \in x, z$ ) due to finite temperature  $T_t$  that leads to a finite spread in coupling  $g$ . The fitted trap location is at  $z_t = 222(16) \text{ nm}$ , agreeing well with the expectation, and the fitted temperature is  $T_t = 113(51) \mu\text{K}$ . The corresponding atom-photon coupling rate is  $g = 2\pi \times 47 \text{ MHz}$  with a standard deviation  $\sigma_g = 2\pi \times 15 \text{ MHz}$ . The extracted trapping probability is  $p = 0.10(3)$ , around 20% of the effectively coupled atom number  $\mathcal{N}t_i \approx 0.56$  in the optical funnel.

In conclusion, we have demonstrated an optical trapping technique that guides and synchronously localizes an atom on a planar nanophotonic resonator with sub-wavelength precision. The observed trapping probability  $\sim 10\%$  is significantly higher than a time-of-flight trapping scheme that requires instantaneous feedback from probing a WGM resonator [25]. To further increase trap loading probability and lifetime, evanescent-wave cooling [42, 43], Raman sideband cooling [44, 45], or cavity cooling [46, 47] may be implemented. The achieved single-atom cooperativity  $\bar{C} \lesssim 1$  is currently limited by the quality factor  $Q \approx 5 \times 10^4$  of the coupled microring circuit. We expect significant improvement in the cooperativity parameter by 20-fold with a better  $Q > 10^6$  [32, 36]. Even stronger atom-photon coupling can be realized in a tunable trap near the waveguide surface [36]. Our work would enable new applications, for example, in chiral quantum optics [20, 21, 48, 49] based on trapped atoms coupled to a WGM resonator. Our system also holds a promise for realizing photon-mediated atom-atom interactions and quantum many-body physics [5, 6, 50–

[53] with multiple trapped atoms.

We thank B. M. Fields and M. E. Kim for their prior contribution to the experiment. This work was supported by the AFOSR (Grant NO. FA9550-17-1-0298) and the

ONR (Grant NO. N00014-17-1-2289). H.T. and C.-L.H. acknowledge support from the NSF (Grant NO. PHY-1848316).

---

[1] D. E. Chang, V. Vuletić, and M. D. Lukin, Quantum nonlinear optics — photon by photon, *Nature Photonics* **8**, 685 (2014).

[2] H. J. Kimble, The quantum internet, *Nature* **453**, 1023 (2008).

[3] A. Reiserer and G. Rempe, Cavity-based quantum networks with single atoms and optical photons, *Rev. Mod. Phys.* **87**, 1379 (2015).

[4] H. Ritsch, P. Domokos, F. Brennecke, and T. Esslinger, Cold atoms in cavity-generated dynamical optical potentials, *Rev. Mod. Phys.* **85**, 553 (2013).

[5] J. S. Douglas, H. Habibian, C.-L. Hung, A. V. Gorshkov, H. J. Kimble, and D. E. Chang, Quantum many-body models with cold atoms coupled to photonic crystals, *Nature Photonics* **9**, 326 (2015).

[6] A. González-Tudela, C.-L. Hung, D. E. Chang, J. I. Cirac, and H. J. Kimble, Subwavelength vacuum lattices and atom–atom interactions in two-dimensional photonic crystals, *Nature Photonics* **9**, 320 (2015).

[7] E. Vetsch, D. Reitz, G. Sagué, R. Schmidt, S. T. Dawkins, and A. Rauschenbeutel, Optical interface created by laser-cooled atoms trapped in the evanescent field surrounding an optical nanofiber, *Phys. Rev. Lett.* **104**, 203603 (2010).

[8] A. Goban, K. S. Choi, D. J. Alton, D. Ding, C. Lacroûte, M. Pototschnig, T. Thiele, N. P. Stern, and H. J. Kimble, Demonstration of a state-insensitive, compensated nanofiber trap, *Phys. Rev. Lett.* **109**, 033603 (2012).

[9] H. L. Sørensen, J.-B. Béguin, K. W. Kluge, I. Iakouporov, A. S. Sørensen, J. H. Müller, E. S. Polzik, and J. Appel, Coherent backscattering of light off one-dimensional atomic strings, *Phys. Rev. Lett.* **117**, 133604 (2016).

[10] N. V. Corzo, B. Gouraud, A. Chandra, A. Goban, A. S. Sheremet, D. V. Kupriyanov, and J. Laurat, Large bragg reflection from one-dimensional chains of trapped atoms near a nanoscale waveguide, *Phys. Rev. Lett.* **117**, 133603 (2016).

[11] P. Solano, P. Barberis-Blostein, F. K. Fatemi, L. A. Orozco, and S. L. Rolston, Super-radiance reveals infinite-range dipole interactions through a nanofiber, *Nature Communications* **8**, 1857 (2017).

[12] N. V. Corzo, J. Raskop, A. Chandra, A. S. Sheremet, B. Gouraud, and J. Laurat, Waveguide-coupled single collective excitation of atomic arrays, *Nature* **566**, 359 (2019).

[13] A. Goban, C.-L. Hung, S.-P. Yu, J. D. Hood, J. A. Muniz, J. H. Lee, M. J. Martin, A. C. McClung, K. S. Choi, D. E. Chang, O. Painter, and H. J. Kimble, Atom–light interactions in photonic crystals, *Nature Communications* **5**, 3808 (2014).

[14] A. Goban, C.-L. Hung, J. D. Hood, S.-P. Yu, J. A. Muniz, O. Painter, and H. J. Kimble, Superradiance for atoms trapped along a photonic crystal waveguide, *Phys. Rev. Lett.* **115**, 063601 (2015).

[15] J. D. Thompson, T. G. Tiecke, N. P. de Leon, J. Feist, A. V. Akimov, M. Gullans, A. S. Zibrov, V. Vuletić, and M. D. Lukin, Coupling a single trapped atom to a nanoscale optical cavity, *Science* **340**, 1202 (2013).

[16] C. Junge, D. O’Shea, J. Volz, and A. Rauschenbeutel, Strong coupling between single atoms and nontransversal photons, *Phys. Rev. Lett.* **110**, 213604 (2013).

[17] T. G. Tiecke, J. D. Thompson, N. P. de Leon, L. R. Liu, V. Vuletić, and M. D. Lukin, Nanophotonic quantum phase switch with a single atom, *Nature* **508**, 241 (2014).

[18] J. Volz, M. Scheucher, C. Junge, and A. Rauschenbeutel, Nonlinear  $\pi$  phase shift for single fibre-guided photons interacting with a single resonator-enhanced atom, *Nature Photonics* **8**, 965 (2014).

[19] S. Kato and T. Aoki, Strong coupling between a trapped single atom and an all-fiber cavity, *Phys. Rev. Lett.* **115**, 093603 (2015).

[20] M. Scheucher, A. Hilico, E. Will, J. Volz, and A. Rauschenbeutel, Quantum optical circulator controlled by a single chirally coupled atom, *Science* **354**, 1577 (2016).

[21] O. Bechler, A. Borne, S. Rosenblum, G. Guendelman, O. E. Mor, M. Netser, T. Ohana, Z. Aqua, N. Drucker, R. Finkelstein, Y. Lovsky, R. Bruch, D. Gurovich, E. Shafir, and B. Dayan, A passive photon–atom qubit swap operation, *Nature Physics* **14**, 996 (2018).

[22] K. P. Nayak, J. Wang, and J. Keloth, Real-time observation of single atoms trapped and interfaced to a nanofiber cavity, *Phys. Rev. Lett.* **123**, 213602 (2019).

[23] D. H. White, S. Kato, N. Német, S. Parkins, and T. Aoki, Cavity dark mode of distant coupled atom-cavity systems, *Phys. Rev. Lett.* **122**, 253603 (2019).

[24] P. Samutpraphoot, T. Đorđević, P. L. Ocola, H. Bernien, C. Senko, V. Vuletić, and M. D. Lukin, Strong coupling of two individually controlled atoms via a nanophotonic cavity, *Phys. Rev. Lett.* **124**, 063602 (2020).

[25] E. Will, L. Masters, A. Rauschenbeutel, M. Scheucher, and J. Volz, Coupling a single trapped atom to a whispering-gallery-mode microresonator, *Phys. Rev. Lett.* **126**, 233602 (2021).

[26] T. Đorđević, P. Samutpraphoot, P. L. Ocola, H. Bernien, B. Grinkemeyer, I. Dimitrova, V. Vuletić, and M. D. Lukin, Entanglement transport and a nanophotonic interface for atoms in optical tweezers, *Science* **373**, 1511 (2021).

[27] D. E. Chang, J. S. Douglas, A. González-Tudela, C.-L. Hung, and H. J. Kimble, Colloquium: Quantum matter built from nanoscopic lattices of atoms and photons, *Rev. Mod. Phys.* **90**, 031002 (2018).

[28] A. S. Sheremet, M. I. Petrov, I. V. Iorsh, A. V. Poshakinskiy, and A. N. Poddubny, Waveguide quantum electrodynamics: collective radiance and photon-photon correlations (2021), [arXiv:2103.06824 \[quant-ph\]](https://arxiv.org/abs/2103.06824).

[29] A. P. Burgers, L. S. Peng, J. A. Muniz, A. C. McClung, M. J. Martin, and H. J. Kimble, Clocked atom delivery to a photonic crystal waveguide, *Proceedings of the Na-*

tional Academy of Sciences **116**, 456 (2019).

[30] J. D. Hood, A. Goban, A. Asenjo-Garcia, M. Lu, S.-P. Yu, D. E. Chang, and H. J. Kimble, Atom–atom interactions around the band edge of a photonic crystal waveguide, *Proceedings of the National Academy of Sciences* **113**, 10507 (2016).

[31] M. E. Kim, T.-H. Chang, B. M. Fields, C.-A. Chen, and C.-L. Hung, Trapping single atoms on a nanophotonic circuit with configurable tweezer lattices, *Nature Communications* **10**, 1647 (2019).

[32] H. Tamura, T.-H. Chang, X. Zhou, B. Fields, M. Zhu, and C.-L. Hung, Microring resonators on a suspended membrane circuit for atom–light interactions, in *Integrated Optics: Devices, Materials, and Technologies XXV*, Vol. 11689, International Society for Optics and Photonics (SPIE, 2021) pp. 174 – 179.

[33] S.-P. Yu, J. A. Muniz, C.-L. Hung, and H. J. Kimble, Two-dimensional photonic crystals for engineering atom–light interactions, *Proceedings of the National Academy of Sciences* **116**, 12743 (2019).

[34] T.-H. Chang, X. Zhou, M. Zhu, B. M. Fields, and C.-L. Hung, Efficiently coupled microring circuit for on-chip cavity QED with trapped atoms, *Applied Physics Letters* **117**, 174001 (2020).

[35] See supplemental material for more experimental and theory details.

[36] T.-H. Chang, B. M. Fields, M. E. Kim, and C.-L. Hung, Microring resonators on a suspended membrane circuit for atom–light interactions, *Optica* **6**, 1203 (2019).

[37] T. Aoki, B. Dayan, E. Wilcut, W. P. Bowen, A. S. Parkins, T. J. Kippenberg, K. J. Vahala, and H. J. Kimble, Observation of strong coupling between one atom and a monolithic microresonator, *Nature* **443**, 671 (2006).

[38] B. K. Teo and G. Raithel, Atom reflection in a tapered magnetic guide, *Phys. Rev. A* **65**, 051401 (2002).

[39] J. Poulin, P. S. Light, R. Kashyap, and A. N. Luiten, Optimized coupling of cold atoms into a fiber using a blue-detuned hollow-beam funnel, *Phys. Rev. A* **84**, 053812 (2011).

[40] We perform trajectory simulations in the  $x$ - $z$  plane. Motion along the  $y$ -axis is less relevant due to symmetry of the waveguide, the large dipole beam waist  $7\ \mu\text{m}$ , and its long Rayleigh length  $z_R \approx 165\ \mu\text{m}$ .

[41] Multiphysics software for optimizing designs.

[42] P. Desbiolles, M. Arndt, P. Sriftgiser, and J. Dalibard, Elementary sisyphus process close to a dielectric surface, *Phys. Rev. A* **54**, 4292 (1996).

[43] Y. B. Ovchinnikov, I. Manek, and R. Grimm, Surface trap for cs atoms based on evanescent-wave cooling, *Phys. Rev. Lett.* **79**, 2225 (1997).

[44] Y. Meng, A. Dareau, P. Schneeweiss, and A. Rauschenbeutel, Near-ground-state cooling of atoms optically trapped 300 nm away from a hot surface, *Phys. Rev. X* **8**, 031054 (2018).

[45] V. Vuletić, C. Chin, A. J. Kerman, and S. Chu, Degenerate raman sideband cooling of trapped cesium atoms at very high atomic densities, *Phys. Rev. Lett.* **81**, 5768 (1998).

[46] P. Maunz, T. Puppe, I. Schuster, N. Syassen, P. W. H. Pinkse, and G. Rempe, Cavity cooling of a single atom, *Nature* **428**, 50 (2004).

[47] M. Hosseini, Y. Duan, K. M. Beck, Y.-T. Chen, and V. Vuletić, Cavity cooling of many atoms, *Phys. Rev. Lett.* **118**, 183601 (2017).

[48] P. Lodahl, S. Mahmoodian, S. Stobbe, A. Rauschenbeutel, P. Schneeweiss, J. Volz, H. Pichler, and P. Zoller, Chiral quantum optics, *Nature* **541**, 473 (2017).

[49] I. Shomroni, S. Rosenblum, Y. Lovsky, O. Bechler, G. Guendelman, and B. Dayan, All-optical routing of single photons by a one-atom switch controlled by a single photon, *Science* **345**, 903 (2014).

[50] S. Gopalakrishnan, B. L. Lev, and P. M. Goldbart, Frustration and glassiness in spin models with cavity-mediated interactions, *Phys. Rev. Lett.* **107**, 277201 (2011).

[51] C.-L. Hung, A. González-Tudela, J. I. Cirac, and H. J. Kimble, Quantum spin dynamics with pairwise-tunable, long-range interactions, *Proceedings of the National Academy of Sciences* **113**, E4946 (2016).

[52] E. J. Davis, G. Bentsen, L. Homeier, T. Li, and M. H. Schleier-Smith, Photon-mediated spin-exchange dynamics of spin-1 atoms, *Phys. Rev. Lett.* **122**, 010405 (2019).

[53] Y. Guo, R. M. Kroese, V. D. Vaidya, J. Keeling, and B. L. Lev, Sign-changing photon-mediated atom interactions in multimode cavity quantum electrodynamics, *Phys. Rev. Lett.* **122**, 193601 (2019).

# Supplementary Material for: Subwavelength precision optical guiding for trapped atoms coupled to a nanophotonic resonator

## Appendix A: Experimental setup

The  $\text{Si}_3\text{N}_4$  microring resonator used in this experiment is fabricated on a transparent  $\text{SiO}_2$ - $\text{Si}_3\text{N}_4$  double-layer membrane, suspended over a large window ( $2 \text{ mm} \times 8 \text{ mm}$ ) on a silicon chip. The open window ensures optical access for conventional laser cooling above the chip and freespace optical guiding adopted in this study. The thickness of the  $\text{SiO}_2$  layer is  $\approx 1.76 \mu\text{m}$  while the bottom  $\text{Si}_3\text{N}_4$  layer is  $\approx 645 \text{ nm}$  thick. As shown in Fig. 1, the microring waveguide width and height are  $\approx 750 \text{ nm}$  and  $\approx 380 \text{ nm}$ , respectively. The waveguide forms a racetrack-shaped ring resonator, with  $15 \mu\text{m}$  bend radius and one  $5 \mu\text{m}$ -long straight part in each side. Microring waveguide circumference is  $\approx 104 \mu\text{m}$ . A bus waveguide couples to the microring in a pulley-shaped coupling region and is end-coupled to two lens fibers for photon input and output (with  $\approx 12\%$  single pass coupling efficiency). The lens fibers are pre-aligned and are epoxied in U-shaped grooves fabricated on the silicon chip. Details about the design and fabrication processes of the microring circuit can be found in Ref. [S1].

The experimental setup for probing interaction between cold atoms and a microring resonator is shown in Fig. S1. After the microring circuit is integrated into the ultrahigh vacuum science chamber, optical fibers are guided out of the chamber via teflon fiber feedthroughs [S2] and are connected to the input and output fiber stages. The input fiber stage accepts three beams (852 nm probe beam, 852 nm locking beam and 849 nm blue WGM beam), whose polarizations are carefully adjusted to excite transverse-magnetic-like whispering-gallery modes (TM WGMs). The 849 nm beam runs continuously while the 852 nm probe and locking beams are pulsed on at different times. A 90:10 fiber beam splitter (BS) is inserted in the input stage for intensity pickup and monitoring. At the output, a volume Bragg grating (VBG) is utilized to filter out the 894 nm component, so that the 852 nm probe photons can be recorded using a single photon counting module (SPCM). A 99:1 fiber BS picks up 1% of the transmitted light for monitoring the 852 nm locking beam, whose frequency is referenced to a cesium vapor cell.

We illuminate the circuit with a 1064 nm external heating beam (up to 300 mW) to thermally tune the microring resonances. Frequency of the probe TM-WGM is thermally stabilized to the  $F = 4 \leftrightarrow F' = 5$  transition via a computer-controlled feedback that monitors the transmission of the locking beam. In each experiment, we pulse on the locking beam immediately following the probe pulses so to stabilize the WGM resonance without affecting the atom-microring coupling. Figure S2(a) shows the transmission spectrum across the probe WGM resonance, where the line center is well-stabilized to within  $\pm 20 \text{ MHz}$  relative to the atomic resonance. The frequency error is around 0.6% of the WGM resonance linewidth, and has negligibly small effect on probing atom-WGM interaction.

Wavelength of the blue WGM,  $\lambda_b = 849.1 \text{ nm}$ , is one free spectral range away from the probe WGM. A small blue-detuned beam power ( $40 \mu\text{W}$ ) is used to excited the blue WGM (at an equivalent circulated power of  $3.2 \text{ mW}$ ) to create a strong repulsive potential near the microring surface; see later discussions. We excite the blue WGM continuously to avoid any transient thermal effect, and keep the probe WGM frequency stabilized during the experiment.

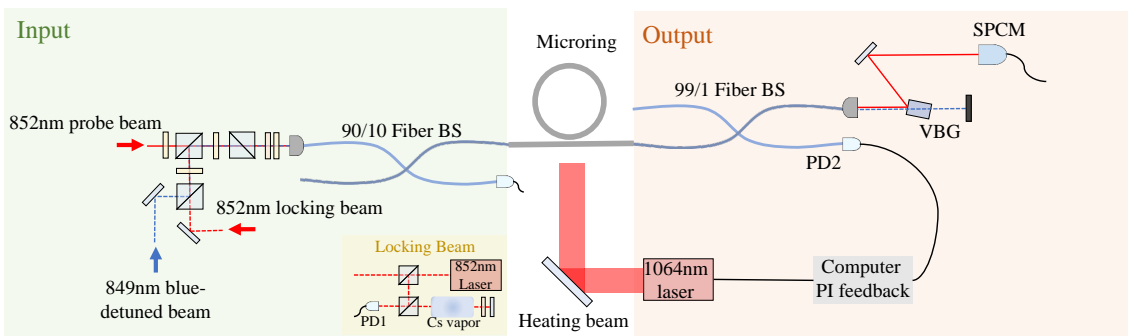


FIG. S1. Experimental setup for probing atom-microring coupling.

## Appendix B: Characterization of the microring resonator

We design the bus waveguide pulley-coupler to achieve near critical-coupling condition, where the waveguide coupling rate  $\kappa_e$  equals the intrinsic photon loss rate  $\kappa_i$ . In reality, a small mismatch would exist and a fiber Mach-Zehnder (MZ) interferometer [Fig. S2(b)] is utilized to determine whether the microring is under-coupled ( $\kappa_e < \kappa_i$ ) or over-coupled ( $\kappa_e > \kappa_i$ ). In the latter case, a  $\pi$  phase shift in the bus waveguide transmission would result, when the probe frequency is swept across a microring resonance. In an unbalanced MZ interferometer with slightly longer arm in the microring path, fringe periodicity will increase (decrease) for under-coupled (over-coupled) condition [Fig. S2(c)]. Figure S2 (d) and (e) show the photodetector reading  $V_{PD}$  of the interferometer output and the extracted peak distances as a function of probe frequency. Comparing with the output far from the microring resonance (d), a clear increase of peak distance is observed in (e) near the microring resonance. This indicates that the microring is in the under-coupled condition.

We fit the transmission spectrum of the microring resonator [Fig. S2(a)], knowing that  $\kappa_e < \kappa_i$ . We extract the external coupling rate  $\kappa_e \approx 2\pi \times 2.3$  GHz and the intrinsic loss rate  $\kappa_i \approx 2\pi \times 4.8$  GHz. The total photon loss rate is  $\kappa_{\text{tot}} \approx 2\pi \times 7.1$  GHz, giving a quality factor  $Q \approx 5 \times 10^4$  for the probe WGM resonance studied in the experiment.

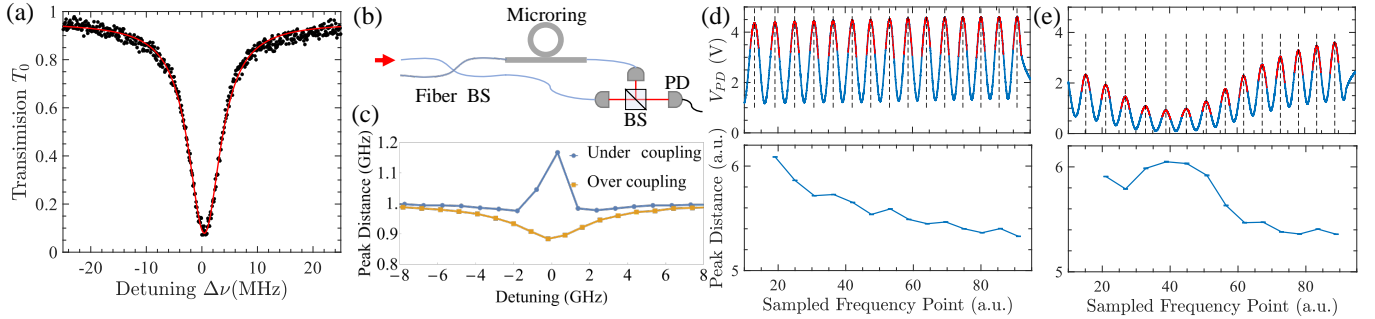


FIG. S2. Characterization of the microring resonator. (a) Transmission spectrum of the bare microring resonator. (b) Interferometer setup for determining the bus waveguide coupling condition. (c) Theoretical prediction of the frequency period of the interferometer for different coupling conditions. (d-e) Experiment data when the sweeping range of the laser frequency does not overlap (d) or overlaps (e) with the microring resonance, respectively.

## Appendix C: Fluorescence imaging longitudinal bounces in the optical funnel

As discussed in the main text (Fig. 2), fluorescence imaging provides complementary information on the dynamics of guided atoms in the optical funnel. The imaging procedure is shown in Fig. S3(b). After polarization gradient cooling (PGC) and a wait time  $\Delta t$ , we switch on the top-illuminating beam to freeze out longitudinal atomic motion in a tight lattice potential, as illustrated in Fig. 4(a) inset, and perform fluorescence imaging [S3]. Atomic fluorescence is collected by a microscope objective (numerical aperture NA = 0.35), and is wavelength- as well as polarization-filtered to remove scattered light from the microring waveguide. We record the image on an electron multiplication charge-coupled device, and monitor the fluorescence counts within a 4-by-4 pixels box ( $3 \times 3 \mu\text{m}^2$  area), as shown in Fig. 1(c). Depth of focus of the objective is  $\sim \pm 10 \mu\text{m}$  and the imaged atomic fluorescence mainly comes from atoms captured at  $z \lesssim 10 \mu\text{m}$  above the microring waveguide.

Measured fluorescence counts versus wait time  $\Delta t$  is shown in Fig. S3(c). Similar to the observed transmission peak in Fig. 2(a), atomic fluorescence clearly shows a maximum at  $\Delta t \approx 3.5\text{ms}$ . Within this hold time, the optical funnel draws the atomic cloud towards the surface at  $z \lesssim 10 \mu\text{m}$ , increasing the number of imaged atoms within the depth of focus. We also note that there is already atomic fluorescence detected at  $\Delta t \approx 0\text{ ms}$ . Whereas, there is no clear initial signal in probe transmission as shown in Fig. 2(a). This suggests we have low atom loading efficiency in the near field region during PGC even with the presence of trapped atoms around  $z \lesssim 10 \mu\text{m}$  in the optical funnel potential.

In addition, atomic fluorescence shows multiple peaks regardless of the presence of a repulsive barrier. This suggests that atoms can bounce off longitudinally within the optical funnel multiple times, and can be guided back towards the surface periodically. Indeed, longitudinal reflection is anticipated in an optical funnel due to transverse atomic motion in a strongly tapered guiding potential [S4], as discussed in the main text. Figure S3(a) shows rapid narrowing of the optical funnel within  $z \lesssim 20 \mu\text{m}$ , where the transverse width of the funnel rapidly drops below  $1 \mu\text{m}$  and reaches  $200 \text{ nm } 1/e^2\text{-halfwidth}$  on the waveguide surface. Our Monte Carlo trajectory calculations confirm that most guided atoms bounce off in this region prior to arriving at the near field. Only those with small transverse kinetic energy and

displacement can enter the near field region. Approaching the waveguide surface, these atoms can still be reflected by the repulsive barrier, if present. Otherwise, they will be attracted to the surface due to Casimir-Polder interactions. Comparing measured fluorescence with and without the repulsive barrier, we find that barrier-reflected atoms are responsible for the increased counts after the first peak (or the first bounce) in Fig. S3(c).

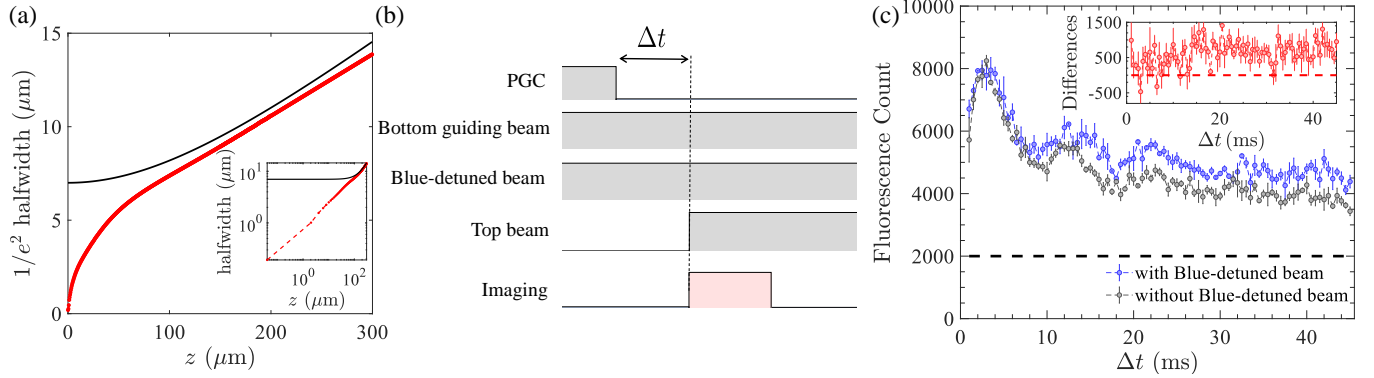


FIG. S3. Analysis of the optical funnel and dynamics of guided atoms observed from fluorescence imaging. (a)  $1/e^2$  halfwidth of the optical funnel (red), comparing with the width of the same beam propagating in free space (black curve). Inset shows the plot in logarithmic scale. (b) Experiment procedure for fluorescence detection. (c) Fluorescence counts as a function of waiting time  $\Delta t$ . Dashed line marks the background. Inset shows the difference in atomic fluorescence with and without the repulsive barrier.

#### Appendix D: Light Shift Calculation and the Casimir-Polder potential

The optical potential experienced by atoms can be separated into contributions from scalar (rank-0), vector (rank-1) and tensor (rank-2) terms in the irreducible tensor representation

$$U(\mathbf{r}) = U^s(\mathbf{r}) + U^v(\mathbf{r}) + U^t(\mathbf{r}) \quad (S1)$$

where

$$U^s(\mathbf{r}) = -\alpha^{(0)}(\omega)|\mathbf{E}(\mathbf{r})|^2 \quad (S2)$$

$$U^v(\mathbf{r}) = -i\alpha^{(1)}(\omega)\frac{\mathbf{E}(\mathbf{r}) \times \mathbf{E}^*(\mathbf{r}) \cdot \hat{\mathbf{F}}}{2F} \quad (S3)$$

$$U^t(\mathbf{r}) = -\alpha^{(2)}(\omega)\frac{3}{F(2F-1)}\left[\frac{\hat{F}_\mu\hat{F}_\nu + \hat{F}_\nu\hat{F}_\mu}{2} - \frac{\hat{\mathbf{F}}^2}{3}\delta_{\mu\nu}\right]E_\mu E_\nu^* \quad (S4)$$

and  $\alpha^{(0,1,2)}(\omega)$  are the corresponding scalar, vector, and tensor polarizabilities,  $\hat{\mathbf{F}}$  is the total angular momentum operator,  $F$  is the quantum number, and  $E_\mu$  ( $\mu \in \{x, y, z\}$ ) are the electric field components in Cartesian coordinates. We calculate the dynamical polarizabilities using transition data summarized in [S5]. TABLE I lists the value of polarizabilities used in the calculation of the trap potential in the main text.

$\lambda$	$\lambda_r$			$\lambda_b$		
	$\alpha^{(0)}$ (a.u.)	$\alpha^{(1)}$ (a.u.)	$\alpha^{(2)}$ (a.u.)	$\alpha^{(0)}$ (a.u.)	$\alpha^{(1)}$ (a.u.)	$\alpha^{(2)}$ (a.u.)
$6S_{1/2} F = 4$	3025	-1625	0	-33519	-29923	0
$6P_{3/2} F' = 5$	3025	3556	5790	15328	47382	-16030

TABLE I. Cesium  $6S_{1/2}, F = 4$  ground state and  $6P_{3/2}, F' = 5$  excited state dynamic polarizabilities at  $\lambda_r = 935.3$  nm and  $\lambda_b = 849.1$  nm.

Relevant light shifts for different Zeeman sub-levels in the  $6S_{1/2}$  ground state and the  $6P_{3/2}$  excited state are shown in Fig. S4. The red-detuned, bottom-illuminating beam (wavelength  $\lambda_r = 935.3$  nm) has linear polarization parallel to the illuminated microring waveguide ( $5\ \mu\text{m}$  straight part of the racetrack), and primarily induces scalar light shift in the ground state, and scalar plus weak tensor light shifts in the excited state; see Fig. S4(b). Moreover,  $\lambda_r = 935.3$  nm

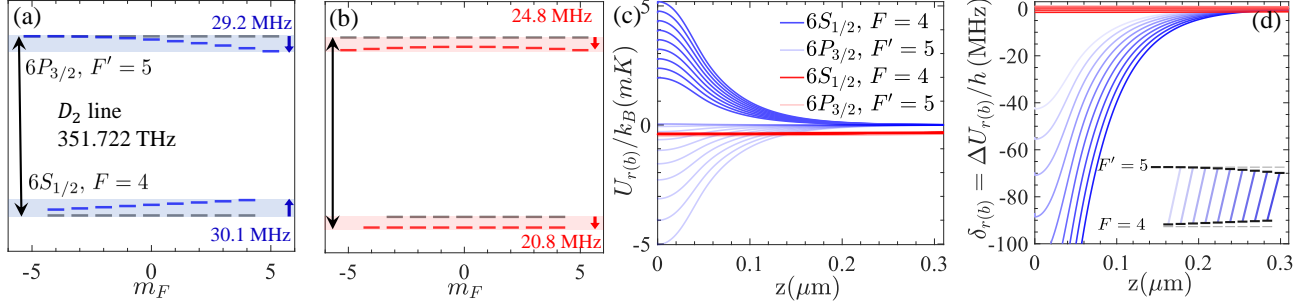


FIG. S4. Total light shifts (sum of scalar, vector and tensor light shifts) caused by (a) the blue WGM ( $\lambda_b = 849.1$  nm,  $\sigma^+$  polarization) and (b) the bottom beam ( $\lambda_r = 935.3$  nm, linearly polarized), with 1 mK (20.8 MHz) shift for the  $m_F = 0$  ground state. Blue (red) lines show the light shifts of different  $m_F$  states and gray lines mark the unperturbed states respectively. Shade bands mark the maximum total light shift. (c) Potential linecuts  $U_r(x = 0, z)$  (red curves) and  $U_b(x = 0, z)$  (blue curves) calculated using powers  $P_r = 15$  mW and  $P_b = 40$   $\mu$ W in the bottom beam and in the blue-detuned beam, respectively. (d) Differential light shifts  $\delta_{r,b}(0, z)$  between the indicated states in the inset, caused by the same bottom beam (red curves) and the ‘blue’ WGM (blue curves) as in (c), respectively.

is a magic wavelength for cesium D2 transition, the differential light shifts between ground and excited states are only caused by small tensor shifts; see Fig. S4(c-d). The blue WGM (wavelength  $\lambda_b = 849.1$  nm) has a locally defined  $\sigma^+$  polarization [see Fig. S5(a)]. It additionally induces vector light shifts in both the ground and the excited states; see Fig. S4(a). For guided atoms in a plugged optical funnel, differential light shifts are mainly caused by the blue WGM [Fig. S4(d)].

In Fig. 1(d), we plot the total potential of a plugged funnel while considering the effect of atom-surface Casimir-Polder interactions. Here, we approximate the ground state Casimir-Polder (CP) potential with  $U_{\text{CP}} = -C_4/z^3(z + \lambda)$ , where  $z$  is atom-surface distance,  $C_4/h = 267$  Hz  $\cdot$   $\mu$ m $^4$ ,  $h$  is the Planck constant and  $\lambda = 136$  nm [S3]. In our trajectory calculations, most guided atoms experience a classical turning point at  $z \gtrsim 100$  nm in a plugged potential. The resulting CP shift is  $\lesssim h \times 1$  MHz and is small compared with light shifts created by the optical funnel.

## Appendix E: Theoretical Models

### 1. Bus waveguide-microring coupling

To model the microring system, we start from the fundamental modes in microring resonator using coupled-mode theory, see details in supplementary material of Ref. [S6]. We denote the amplitude of two fundamental transverse-magnetic (TM) modes as  $a$  for clockwise (CW) mode and  $b$  for counter-clockwise (CCW) mode. The resonator field can be decomposed into these two counter-propagating modes of interest  $\mathbf{E}(r, t) = a\mathbf{E}_+(r, t) + b\mathbf{E}_-(r, t)$ , where  $\mathbf{E}_\pm(r, t) = \mathbf{E}_\pm(r)e^{-i\omega t}$  and

$$\mathbf{E}_\pm(\mathbf{r}) = \left[ \mathcal{E}_\rho(\rho, z)\hat{\rho} \pm i\mathcal{E}_\phi(\rho, z)\hat{\phi} + \mathcal{E}_z(\rho, z)\hat{z} \right] e^{\pm im\phi}. \quad (\text{S1})$$

Here,  $\mathcal{E}_\mu(\rho, z)$  ( $\mu = \rho, \phi, z$ ) are real functions independent of  $\phi$  due to cylindrical symmetry. In our experiment, we excite the resonator mode by sending light from one end of the bus waveguide. We have the following coupled rate equations

$$\begin{aligned} \frac{da}{dt} &= -\left(\frac{\kappa}{2} + i\Delta_c\right)a(t) + i\beta e^{i\xi}b(t) + i\sqrt{\kappa_e}s_{\text{in}} \\ \frac{db}{dt} &= -\left(\frac{\kappa}{2} + i\Delta_c\right)b(t) + i\beta e^{-i\xi}a(t) \end{aligned} \quad (\text{S2})$$

where  $\Delta_c = \omega_c - \omega$  is the resonator detuning relative to the driving field,  $\beta$  is the coherent back-scattering rate and  $\xi$  is the phase.  $s_{\text{in}}$  is normalized amplitude of the input power in the bus waveguide so that  $P_{\text{in}} = \hbar\omega|s_{\text{in}}|^2$ . The

steady-state mode amplitudes are

$$\begin{aligned} a &= i\sqrt{\kappa_e} \frac{(\frac{\kappa}{2} + i\Delta_c)s_{\text{in}}}{(\frac{\kappa}{2} + i\Delta_c)^2 + \beta^2} \\ b &= i\sqrt{\kappa_e} \frac{i\beta e^{-i\xi}s_{\text{in}}}{(\frac{\kappa}{2} + i\Delta_c)^2 + \beta^2} \end{aligned} \quad (\text{S3})$$

From our characterization of microring [Fig. S2(a)], the back-scattering rate  $\beta$  is much smaller than the linewidth of the cavity, so we neglect it and set  $\beta = 0$ . In this case,  $b = 0$  and we only excite the CW mode with amplitude  $a$ . The transmission spectrum of a bare microring is then

$$T_0(\Delta_c) = \left| 1 + i\sqrt{\kappa_e} \frac{a}{s_{\text{in}}} \right|^2 = \left| 1 - \frac{2\kappa_e}{\tilde{\kappa}} \right|^2, \quad (\text{S4})$$

where  $\tilde{\kappa} = \kappa + 2i\Delta_c$ . This is the formula we used for fitting the transmission spectrum of a bare resonator.

## 2. Atom-WGM photon coupling

We now consider atom-WGM photon coupling. In cavity QED, single atom-photon coupling strength is defined as

$$g_i = d_i \sqrt{\frac{\omega}{2\hbar\epsilon_0 V_m}} \quad (\text{S5})$$

where  $d_i = \langle e|\mathbf{d}|g\rangle \cdot \mathbf{e}_i$  is the transition dipole moment,  $i$  labels  $\sigma^\pm$  or  $\pi$  transitions,  $\mathbf{e}_i$  is the polarization unit vector,  $\hbar$  is the reduced Planck's constant,  $\epsilon_0$  is the vacuum permittivity, and  $V_m(\mathbf{r}_a)$  is the effective mode volume at atomic position  $\mathbf{r}_a = (\rho_a, \phi_a, z_a)$ ,

$$V_m(\rho_a, z_a) = \frac{\int \epsilon(\rho, z) |\mathbf{E}_\pm(\rho, z)|^2 \rho d\rho dz d\phi}{\epsilon(\rho_a, z_a) |\mathbf{u}_i \cdot \mathbf{E}_\pm(\rho_a, z_a)|^2}. \quad (\text{S6})$$

As shown in Fig. S5(a), the TM WGM is nearly circularly polarized above the waveguide because of strong confinement of the electric field. Polarization rotation of the WGM is also locked to the circulation direction. We can thus consider a case that the atomic spin axis is aligned transversely to the microring waveguide, and CW (CCW) WGM photons would locally drive only the  $\sigma^+$  ( $\sigma^-$ ) transition, as shown in Fig. S5. In the case that an atom is spin-polarized to the  $|F = 4, m_F = 4\rangle$  ground state, the atom-CW WGM photon coupling strength  $g_a$  can be maximized for the  $|F = 4, m_F = 4\rangle \leftrightarrow |F' = 5, m_{F'} = 5\rangle$  cycling transition,

$$g = \sqrt{\frac{3\lambda^3\omega\gamma}{16\pi^2V_m}}, \quad (\text{S7})$$

where we have used  $d^2 = \frac{3\lambda^3\epsilon_0\hbar\gamma}{8\pi^2}$ ,  $\lambda$  is the transition wavelength, and  $\gamma$  is the atomic decay rate in free space. Generally, the atom-CW(CCW) WGM photon coupling strength  $g_a$  ( $g_b$ ) for a  $|F = 4, m_F = l\rangle$  ground state can be written as

$$g_a = \eta_l^+ g \quad (\text{S8})$$

$$g_b = \eta_l^- g \quad (\text{S9})$$

where  $\eta_l^\pm = \sqrt{2}C_{l,l\pm 1}$  and  $C_{l,l\pm 1}$  is the dipole matrix element for the  $\sigma^{+(-)}$  transition [S7]. For example,  $\eta_4^- = 1/\sqrt{45}$  for the  $|F = 4, m_F = 4\rangle \leftrightarrow |F' = 5, m_{F'} = 3\rangle$  transition.

In Fig. 3(a), we plot the averaged  $\bar{g}$  of all magnetic sub-levels for the atom-WGM photon coupling. Here  $\bar{g}^2 \equiv \langle g_a^2 \rangle = \langle g_b^2 \rangle$ , and the averaged cooperativity  $\bar{C} \equiv 4\bar{g}^2/\kappa/\gamma = \langle C^+ \rangle = \langle C^- \rangle$ , where  $C^{+(-)} = 4g_{a(b)}^2/\kappa/\gamma$  is the cooperativity for atom-CW (CCW) WGM photon coupling, and  $\langle \dots \rangle$  denotes averaging over all magnetic sub-levels.

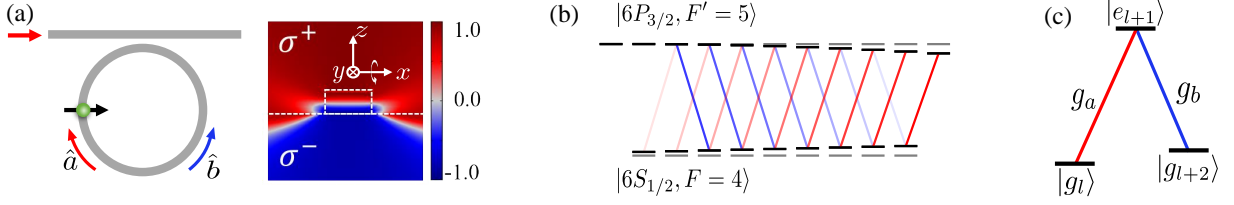


FIG. S5. (a) Degree of circular polarization of the CW WGM (mode  $\hat{a}$ ) locally around the microring waveguide, calculated as  $(|\mathbf{E}_+ \cdot \mathbf{e}_+^*|^2 - |\mathbf{E}_+ \cdot \mathbf{e}_-^*|^2)/|\mathbf{E}_+|^2$ , and  $\mathbf{e}_\pm = (\mathbf{e}_y \pm i\mathbf{e}_z)/\sqrt{2}$ . Note the mode propagation is along the  $y$ -axis, but the circular polarization is about the  $x$ -axis. (b) Multilevels of the  $|F=4\rangle \leftrightarrow |F'=5\rangle$  transition. (c) Effective  $\Lambda$ -level and related coupling ( $|g_l\rangle \leftrightarrow |e_{l+1}\rangle \leftrightarrow |g_{l+2}\rangle$ ).

### 3. Transmission spectrum of coupled atom-microring-bus waveguide system

We calculate the transmission spectrum in the weak driving limit, by solving for the transmission coefficient of single photon transport in the atom-coupled microring system. For completeness, we consider a multi-level atom coupled to both of the CW and CCW WGMs, and adopt a real-space representation for discussing single photon transport in the system [S8–S10]. Including dissipation in the WGMs and the atomic excited states, we consider a non-Hermitian Hamiltonian in the quantum-jump approach [S11]:

$$\hat{H}_{\text{eff}}/\hbar = \left( \omega_c - i\frac{\kappa_i}{2} \right) (\hat{a}^\dagger \hat{a} + \hat{b}^\dagger \hat{b}) + \int dx \hat{c}_R^\dagger(x) \left( \omega_0 - iv_g \frac{\partial}{\partial x} \right) \hat{c}_R(x) + \int dx \hat{c}_L^\dagger(x) \left( \omega_0 + iv_g \frac{\partial}{\partial x} \right) \hat{c}_L(x) + \int dx \delta(x) \left[ V_a \hat{c}_R^\dagger(x) \hat{a} + V_a^* \hat{c}_R(x) \hat{a}^\dagger \right] + \int dx \delta(x) \left[ V_b \hat{c}_L^\dagger(x) \hat{b} + V_b^* \hat{c}_L(x) \hat{b}^\dagger \right] + \sum_l \left( \Omega_{e_l} - i\frac{\gamma}{2} \right) |e_l\rangle \langle e_l| + \sum_l \Omega_{g_l} |g_l\rangle \langle g_l| + g \sum_l \left[ \eta_l^+ \left( \hat{a} \hat{\sigma}_{+,l}^\dagger + \hat{a}^\dagger \hat{\sigma}_{+,l} \right) + \eta_l^- \left( \hat{b} \hat{\sigma}_{-,l}^\dagger + \hat{b}^\dagger \hat{\sigma}_{-,l} \right) \right], \quad (\text{S10})$$

where the terms in the first two lines describe the bus waveguide-coupled microring system with degenerate CW and CCW modes of resonant frequency  $\omega_c$ ,  $\hat{a}^{(\dagger)}$  [ $\hat{b}^{(\dagger)}$ ] are the creation (annihilation) operators of CW [CCW] WGM photons,  $\hat{c}_R^{(\dagger)}(x)$  [ $\hat{c}_L^{(\dagger)}(x)$ ] creates (annihilates) a right-moving [left-moving] photon at position  $x$  in the bus waveguide with frequency near  $\omega_0$ ,  $v_g$  is the group velocity of the waveguide mode,  $V_{a(b)} = i\sqrt{\kappa_e v_g}$  is the waveguide-microring coupling strength, and  $\delta(x)$  is the Dirac delta function. The third line describes a multi-level atom, as illustrated in Fig. S5, and its coupling to the CW and CCW WGMs, where  $\Omega_{e_l}$  ( $\Omega_{g_l}$ ) is a excited (ground) state energy,  $l$  labels the magnetic quantum number, and  $\hat{\sigma}_{\pm,l} \equiv |g_l\rangle \langle e_{l\pm 1}|$  is the lowering operator for the corresponding atom-CW (CCW) WGM coupling.

We consider an atom initially in an arbitrary state  $|\Phi(t \rightarrow -\infty)\rangle = \sum_l \alpha_l |g_l\rangle$ , and the waveguide is injected with a right propagating photon. In the single excitation limit, evolution of the state should generally take the form

$$|\Phi(t)\rangle = \sum_l \int dx \left( \tilde{\phi}_{R,l} \hat{c}_R^\dagger(x) + \tilde{\phi}_{L,l} \hat{c}_L^\dagger(x) \right) |0\rangle |g_l\rangle + \sum_l \tilde{\epsilon}_{e_l} |0\rangle |e_l\rangle + \tilde{\epsilon}_{a,g_l} \hat{a}^\dagger |0\rangle |g_l\rangle + \tilde{\epsilon}_{b,g_l} \hat{b}^\dagger |0\rangle |g_l\rangle, \quad (\text{S11})$$

where  $|0\rangle$  represents the vacuum state in both the microring and the waveguide, and  $(\tilde{\phi}_{R,l}, \tilde{\phi}_{L,l}, \tilde{\epsilon}_{e_l}, \tilde{\epsilon}_{a,g_l}, \tilde{\epsilon}_{b,g_l})$  are time-dependent coefficients. We can solve for the state evolution  $|\Phi(t)\rangle$  using the Schrödinger equation  $i\hbar \frac{\partial}{\partial t} |\Phi(t)\rangle = \hat{H}_{\text{eff}} |\Phi(t)\rangle$  and the effective Hamiltonian Eq. (S10). However, we are primarily interested in finding the bus waveguide transmission, and thus the value  $\langle \Phi(t_d) | \hat{c}_R^\dagger(x_d) \hat{c}_R(x_d) | \Phi(t_d) \rangle$ , where the detection point can be taken to infinity  $x_d \rightarrow \infty$  and  $t_d \rightarrow \infty$ . We then focus on finding the solution  $|\Phi(t)\rangle = \sum_l e^{-i\epsilon_l t} |E_l\rangle$ , where the state is written as a superposition of stationary states  $|E_l\rangle$ , each satisfying  $\hat{H}_{\text{eff}} |E_l\rangle = E_l |E_l\rangle$ . We find that

$$|E_l\rangle = \int dx \left( \phi_{R,l} \hat{c}_R^\dagger(x) |g_l\rangle + \phi_{L,l+2} \hat{c}_L^\dagger(x) |g_{l+2}\rangle \right) |0\rangle + \epsilon_{e_{l+1}} |e_{l+1}\rangle + \epsilon_{a,g_l} \hat{a}^\dagger |0\rangle |g_l\rangle + \epsilon_{b,g_{l+2}} \hat{b}^\dagger |0\rangle |g_{l+2}\rangle, \quad (\text{S12})$$

and  $E_l = \omega + \Omega_{g_l}$ , where  $\omega = \omega_0 + v_g k$  is the input photon frequency;  $\phi_{R,l}(x) = \alpha_l e^{ikx} [\theta(-x) + t_l \theta(x)]$ , and  $\phi_{L,l+2}(x) = \alpha_l r_l e^{-ik_l' x} \theta(-x)$  describe the right- and left-propagating photon wavefunctions in the bus waveguide,

respectively, where  $k'_l = k + (\Omega_{g_l} - \Omega_{g_{l+2}})/v_g$ , and  $\theta(x)$  is the Heaviside step function. Effectively, the system could be described by a collection of  $\Lambda$ -levels ( $|g_l\rangle \leftrightarrow |e_{l+1}\rangle \leftrightarrow |g_{l+2}\rangle$ ) in the single excitation limit, each giving transmission and reflection coefficients for the right-propagating input photon as

$$t_l(\omega, g) = 1 - \frac{2\kappa_e}{\tilde{\kappa}} \frac{1 + \tilde{C}_l^-}{1 + \tilde{C}_l^+ + \tilde{C}_l^-} \quad (\text{S13})$$

$$r_l(\omega, g) = \frac{2\kappa_e}{\tilde{\kappa}} \frac{\eta_l^+}{\eta_{l+2}^-} \frac{\tilde{C}_l^-}{1 + \tilde{C}_l^+ + \tilde{C}_l^-}, \quad (\text{S14})$$

where  $\tilde{C}_l^+ = \frac{4|\eta_l^+ g|^2}{\tilde{\kappa}\tilde{\gamma}_l}$  and  $\tilde{C}_l^- = \frac{4|\eta_{l+2}^- g|^2}{(\tilde{\kappa} + i\delta_l/2)\tilde{\gamma}_l}$  are complex cooperativities for  $\sigma^+$  and  $\sigma^-$  transitions in the  $l$ -th  $\Lambda$ -level, respectively,  $\tilde{\kappa} = \kappa + 2i\Delta_c$ ,  $\tilde{\gamma}_l = \gamma + 2i(\Omega_{e_{l+1}} - \Omega_{g_l} - \omega)$ , and  $\delta_l = \Omega_{g_{l+2}} - \Omega_{g_l}$  is the ground state splitting. For  $l = F$  and  $F - 1$  states,  $\eta_{l+2}^- = 0$ ,  $\tilde{C}_l^- = 0$ , and  $r_l = 0$  due to the lack of coupling to the CCW WGM. The total transmission for an atom in state  $|\Phi(t \rightarrow -\infty)\rangle = \sum_l \alpha_l |g_l\rangle$  is thus

$$\mathcal{T}(\omega, g) = \lim_{x_d, t_d \rightarrow \infty} \left| \langle \Phi(t_d) | c_R^\dagger(x_d) c_R(x_d) | \Phi(t_d) \rangle \right|^2 = \sum_l \alpha_l^2 |t_l|^2, \quad (\text{S15})$$

and the transmission is the sum of contributions from individual  $\Lambda$ -levels.

We note that the coupling to CW and CCW WGMs are asymmetric in the Zeeman manifold. Assuming equal population in the  $F = 4$  magnetic sub-levels and no Zeeman energy splitting, we have  $\langle \tilde{C}_l^- \rangle = \frac{28}{55} \langle \tilde{C}_l^+ \rangle \approx 0.5 \langle \tilde{C}_l^+ \rangle$ . We have used this relation for rough estimate of peak transmission  $\mathcal{T}/T_0 \approx 2.9$  in Fig. 3 without considering light shifts.

Moreover, in the case of an atom fully polarized in the stretched state,  $|F = 4, m_F = 4\rangle$ , transmission spectrum simplifies to

$$\mathcal{T}(\omega, g) = |t|^2 = \left| 1 - \frac{2\kappa_e}{\tilde{\kappa}(1 + \tilde{C})} \right|^2, \quad (\text{S16})$$

and reflectivity  $|r|^2 = 0$ . Here  $\tilde{C} = 4\frac{g^2}{\tilde{\kappa}\tilde{\gamma}}$ ,  $\tilde{\gamma} = \gamma + 2i\Delta_a$ , and  $\Delta_a = \omega_a - \omega$  is the photon detuning from transition frequency  $\omega_a$ . In a no-atom case,  $\tilde{C} = 0$  and the transmission  $\mathcal{T}(\omega, 0)$  further reduces to that of Eq. (S4).

## Appendix F: Fitting procedure for guided atoms

We use Eqs. (S15) and (S16) to fit the transmission spectrum of unpolarized guided atoms and spin-polarized trapped atoms, respectively. For guided atoms, we calculate a time-averaged transmission spectrum since atom-WGM photon interaction occurs during an atom in transit through the near field, and the coupling strength  $g$  and the atomic energy levels ( $\Omega_{e_l}, \Omega_{g_l}$ ) are position dependent. We incorporate trajectory and light shift calculations to obtain an ensemble of time-dependent  $(g(t), \Omega_{e_l}(t), \Omega_{g_l}(t))$ . This allows us to calculate the averaged transmission with the occurrence of  $\mathcal{N}$  atom-transits during the 1 ms probe window. Using Eq. (S15) and (S13), we calculate

$$\frac{T(\omega)}{T_0} = 1 + \mathcal{N} \left[ \frac{\int dt \mathcal{T}(\omega, g(t))}{\int dt \mathcal{T}(\omega, 0)} - 1 \right], \quad (\text{S17})$$

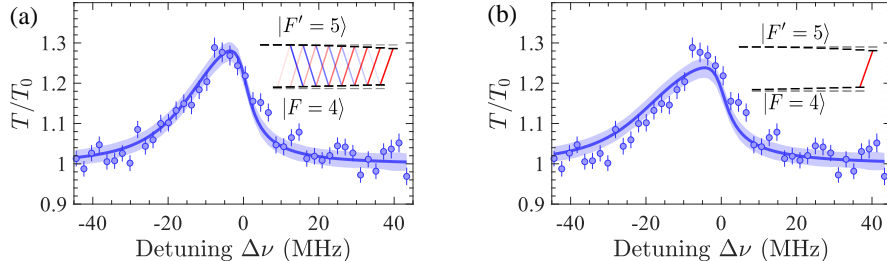


FIG. S6. Fitting transmission spectrum using Eq. (S17), assuming (a) unpolarized and (b) spin-polarized population as illustrated in the insets. Shaded area shows 95% pointwise confidence band.

where  $\langle \dots \rangle$  denotes ensemble averaging over all simulated trajectories. Since the guided atoms are unpolarized, we have assumed equal population in all  $m_F$  states. This model assumes  $\mathcal{N}$  as the only fit parameter, and captures the spectral line shape very well as shown in Figs. 3 and S6(a). For comparison, we have also performed fitting assuming a spin-polarized population in the  $|F = 4, m_F = 4\rangle$  ground state, as shown in Fig. S6(b). The fitted atom flux is  $\mathcal{N} = 65(2) \text{ ms}^{-1}$ , although with worse agreement with the measured line shape.

---

[S1] T.-H. Chang, X. Zhou, M. Zhu, B. M. Fields, and C.-L. Hung, Efficiently coupled microring circuit for on-chip cavity QED with trapped atoms, *Applied Physics Letters* **117**, 174001 (2020).

[S2] E. R. Abraham and E. A. Cornell, Teflon feedthrough for coupling optical fibers into ultrahigh vacuum systems, *Applied optics* **37**, 1762 (1998).

[S3] M. E. Kim, T.-H. Chang, B. M. Fields, C.-A. Chen, and C.-L. Hung, Trapping single atoms on a nanophotonic circuit with configurable tweezer lattices, *Nature Communications* **10**, 1647 (2019).

[S4] B. K. Teo and G. Raithel, Atom reflection in a tapered magnetic guide, *Phys. Rev. A* **65**, 051401 (2002).

[S5] F. Le Kien, P. Schneeweiss, and A. Rauschenbeutel, Dynamical polarizability of atoms in arbitrary light fields: general theory and application to cesium, *The European Physical Journal D* **67**, 92 (2013).

[S6] T.-H. Chang, B. M. Fields, M. E. Kim, and C.-L. Hung, Microring resonators on a suspended membrane circuit for atom-light interactions, *Optica* **6**, 1203 (2019).

[S7] D. A. Steck, *Cesium D line data* (2003).

[S8] J.-T. Shen and S. Fan, Theory of single-photon transport in a single-mode waveguide. i. coupling to a cavity containing a two-level atom, *Phys. Rev. A* **79**, 023837 (2009).

[S9] J.-T. Shen and S. Fan, Theory of single-photon transport in a single-mode waveguide. ii. coupling to a whispering-gallery resonator containing a two-level atom, *Phys. Rev. A* **79**, 023838 (2009).

[S10] T. Li, A. Miranowicz, X. Hu, K. Xia, and F. Nori, Quantum memory and gates using a  $\Lambda$ -type quantum emitter coupled to a chiral waveguide, *Phys. Rev. A* **97**, 062318 (2018).

[S11] H. J. Carmichael, *Statistical methods in quantum optics 2: Non-classical fields* (Springer Science & Business Media, 2009).